

Remote sensing of breaking wave phase speeds with application to non-linear depth inversions

Patricio A. Catálan^{*,1}, Merrick C. Haller

Coastal & Ocean Engineering Program, School of Civil and Construction Engineering, Oregon State University, 220 Owen Hall, Corvallis, OR 97331, USA

Received 29 August 2006; received in revised form 7 July 2007; accepted 5 September 2007

Available online 22 October 2007

Abstract

A number of existing models for surface wave phase speeds (linear and non-linear, breaking and non-breaking waves) are reviewed and tested against phase speed data from a large-scale laboratory experiment. The results of these tests are utilized in the context of assessing the potential improvement gained by incorporating wave non-linearity in phase speed based depth inversions. The analysis is focused on the surf zone, where depth inversion accuracies are known to degrade significantly. The collected data includes very high-resolution remote sensing video and surface elevation records from fixed, in-situ wave gages. Wave phase speeds are extracted from the remote sensing data using a feature tracking technique, and local wave amplitudes are determined from the wave gage records and used for comparisons to non-linear phase speed models and for non-linear depth inversions. A series of five different regular wave conditions with a range of non-linearity and dispersion characteristics are analyzed and results show that a composite dispersion relation, which includes both non-linearity and dispersion effects, best matches the observed phase speeds across the domain and hence, improves surf zone depth estimation via depth inversions. Incorporating non-linearity into the phase speed model reduces errors to $O(10\%)$, which is a level previously found for depth inversions with small amplitude waves in intermediate water depths using linear dispersion. Considering the controlled conditions and extensive ground truth, this appears to be a practical limit for phase speed-based depth inversions. Finally, a phase speed sensitivity analysis is performed that indicates that typical nearshore sand bars should be resolvable using phase speed depth inversions. However, increasing wave steepness degrades the sensitivity of this inversion method.

© 2007 Elsevier B.V. All rights reserved.

Keywords: Phase speeds; Surf zone; Breaking waves; Depth inversions; Remote sensing

1. Introduction

In the coastal zone, spatial variations in the sea bottom influence both the direction and speed of propagation of surface gravity waves. In the modeling of nearshore areas, wave phase speeds and directions are important parameters because wave-averaged nearshore circulation models require their explicit prediction for the determination of radiation stress forcing. Typical existing models for wave phase speeds are based on a prescribed wave form such as sinusoidal, cnoidal, etc.; but, in areas near the onset of wave breaking, wave shape is of non-permanent form and can change very quickly, which makes the

specification of phase speed in this region ambiguous. In addition, most phase speed models are derived explicitly for either breaking or non-breaking waves. Thus, for domains that span the shoaling and breaking zones they are not universally applicable and empirical formulations must often be called upon (e.g. Hedges, 1976; Kirby and Dalrymple, 1986).

Surface wave phase speed is also an important remote sensing observable. For example, if a functional relationship between water depth and phase speed is specified, then remote sensing data can be used to determine bathymetry through depth inversion techniques (e.g. Williams, 1946; Bell, 1999; Stockdon and Holman, 2000). Due to the large footprint of remote sensing observations and considering the comparative difficulties and expense of collecting data by in-situ means, this is a potentially powerful technique for retrieving bathymetry. However, it is clear that in realistic situations the functional relationship between water depth and phase speed is complex and dependent on wave non-linearity, which is a more difficult quantity to observe remotely. In addition,

^{*} Corresponding author.

E-mail addresses: catalapa@engr.orst.edu, patricio.catalan@usm.cl (P.A. Catálan), haller@engr.orst.edu (M.C. Haller).

¹ Also at: Departamento de Obras Civiles, Universidad Tecnica Federico Santa Maria, Valparaiso, Chile.

it is disadvantageous to require separate phase speed models for the regions outside and inside the surf zone, since this likely requires additional gymnastics to determine where to apply each model for a given domain and data set. Aarninkhof et al. (2005) have pursued an alternative track of relating breaking-induced dissipation to the bathymetry. However, the approach still relies on a characterization of the energy flux, which is related to the phase speed. Hence, since the accuracy of depth inversions is directly tied to the accuracy of the phase speed model, there is clearly a need for a general surface wave phase speed model that is applicable from the shoaling zone through the surf zone to the shoreline. Yet, it is not clear that such a model exists.

The accuracy of depth inversions based on remote measurements is dependent on two criteria: 1) the ability of the remote sensor to measure phase speed and wave amplitude, and 2) the applicability of the chosen phase speed (and depth inversion) model to the given wave conditions. The purpose of this paper is to directly compare phase speed models that include non-linear and dispersive effects with remotely sensed phase speed measurements. It is also to study the potential improvement in depth inversion when measured finite amplitude effects are included in the relationship between the measured phase speed and the local water depth. The analysis utilizes a combination of remotely sensed video intensity data and in-situ measurements of free surface elevations. With respect to previous depth inversion studies, the present data set provides remote sensing data at much higher resolution than previously considered, which reduces the amount of inherent smoothing that often occurs in field situations. In addition, the laboratory setting allows us to control the wave conditions and to measure them with high accuracy throughout the surf zone. Finally, we concentrate on the surf zone (though not necessarily shallow water) because the accuracy of depth inversions has been found to significantly degrade in this region.

This paper is organized as follows: in Section 2 we perform a comprehensive review of existing phase speed models. Section 3 describes the measurement techniques and experimental conditions used in this study. Phase speed results and the application of selected phase speed models to depth inversions are given in Section 4. Section 5 provides a discussion of possible error sources and an analysis of the sensitivity of phase speed-based depth inversions to the amplitude of a given bottom perturbation, such as a sand bar. Conclusions are given in Section 6.

2. Phase speeds

2.1. Models for non-breaking waves

The speed of propagation (phase speed or celerity) of surface gravity waves, c , can be defined for a surface of permanent form based on the elapsed time τ required for the surface to travel a characteristic distance l . Then, the phase speed is defined as

$$c = \frac{l}{\tau}. \quad (1)$$

Various permanent form solutions for c can be obtained from surface gravity wave theory. Their form is dependent on the

assumptions made in the description of the underlying wave motion.

2.1.1. Linear theory

The simplest case is from linear wave theory, under the assumption of small wave amplitude and locally horizontal bottom. The resulting free surface can be expressed as $\eta = A \exp \{i(kx - \sigma t)\}$, where $k = 2\pi/L$ is the wavenumber, $\sigma = 2\pi/T$ is the radian frequency, A is the wave amplitude and the quantity $i(kx - \sigma t)$ is the phase. Choosing the wavelength, L , as the characteristic distance (l) the wave period T is then the characteristic time (τ). For linear waves, c , σ , and k are related by means of the linear dispersion relation

$$c^2 = \frac{\sigma^2}{k^2} = \frac{L^2}{T^2} = \frac{g}{k} \tanh(kh), \quad (2)$$

where h is the water depth, g is the gravitational acceleration, and k is the magnitude of the wavenumber vector \mathbf{k} . Here, c is defined relative to a fixed frame of reference. Despite its simplicity, Eq. (2) has proven useful in a number of cases. For example, in intermediate depths and moderate wave heights, the full linear dispersion relation (including currents) has been used to estimate water depths and mean currents with errors as low as $O(5\%)$ (e.g. Dugan et al., 2001; Piotrowski and Dugan, 2002).

However, we are mostly concerned here with waves in the surf zone, and in shallow water ($kh < \pi/10$) Eq. (2) reduces to the simple form

$$c = \sqrt{gh}, \quad (3)$$

which shows a direct relation between the local water depth and the speed. This makes it very simple to use for depth inversion; yet, comparisons with measured data have shown that this linear shallow water approximation underpredicts the observed phase speeds, both in the field (e.g. Inman et al., 1971; Thornton and Guza, 1982; Stockdon and Holman, 2000; Holland, 2001) and in the laboratory (e.g. Svendsen and Buhr Hansen, 1976; Svendsen et al., 1978; Stive, 1980; Stansell and MacFarlane, 2002). In some of these laboratory cases a limited degree of non-linearity was incorporated by including the measured wave setup in the water depth used in Eq. (3) (Svendsen et al., 1978; Stive, 1980), but the overall behavior was still an under-prediction of the phase speeds. In addition, using on a large amount of field data from a cross-shore array of pressure sensors, Holland (2001) showed that, in shallow water, errors in estimated depths using the linear dispersion relation commonly exceeded 50% and were correlated with the offshore wave height. This was a clear indication of the importance of finite amplitude effects for depth inversions.

2.1.2. Boussinesq wave theory

So it is recognized that, while Eq. (3) is non-dispersive (i.e. all waves travel at the same speed), in reality the wave amplitude and the relative water depth will also affect the phase speed. These effects are termed amplitude dispersion and frequency dispersion, respectively (for a thorough review see Svendsen (2006)). Frequency dispersion effects are explicitly

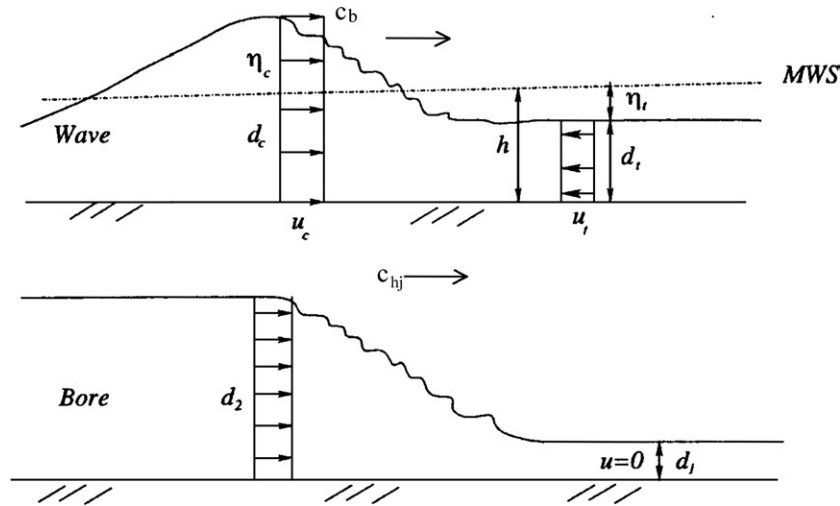


Fig. 1. Schematic of a breaking wave and a hydraulic jump (bore) (Svendsen et al., 2003).

related to the parameter $\mu = kh$, amplitude dispersion to $\delta = A/h$, and a measure of the relative importance of each effect is given by the Ursell number

$$Ur = \frac{\delta}{\mu^2} \propto \frac{kH}{(kh)^3}. \quad (4)$$

The classical Boussinesq wave equations are based on the assumption of $\delta = O(\mu^2) \ll 1$ (weakly dispersive, weakly non-linear); hence, $Ur \sim O(1)$ (Peregrine, 1967). For the case of waves traveling in only one direction, an analytical solution for periodic waves of constant form (cnoidal waves) is given by (e.g. Svendsen, 2006)

$$c = \sqrt{gh \left[1 + \frac{H}{mh} \left(2 - m - 3 \frac{E}{K} \right) \right]}, \quad (5)$$

where H is the wave height; K , E are the complete elliptic functions of the first and second kind, respectively. The parameter m is the modulus of the elliptic functions and can be calculated if the Ursell number is known using

$$Ur = \frac{16}{3} mK^2. \quad (6)$$

Svendsen and Buhr Hansen (1976) rewrote the above equation as

$$c = \sqrt{gh(1 + f(m)H/h)}, \quad (7)$$

which emphasizes the fact that deviations from the linear shallow water speed are expected to be of $O(\delta)$, since $H/h = O(\delta)$, although frequency dispersion effects are still incorporated through the parameter m (Svendsen, 2006). Those authors tested Eq. (7) against phase speeds measured in a laboratory experiment on a planar beach. They showed that the cnoidal theory had problems near the breaking point, where waves sped up and changed form rapidly, but performed better than linear theory shoreward of the point where $h/L_o < 0.10$. This limit is in agreement with the theoretical requirement for cnoidal theory accuracy, $h/L_o < 3/8\pi$ (Svendsen, 1974; Dingemans, 1997).

The depth inversion studies of Holland (2001) and Bell et al. (2004) did not explicitly test phase speed models, but were inherently based on Eq. (7) with a single value for $f(m)$ prescribed throughout the nearshore domain. Holland (2001) chose an $f(m)$ value that gave the best agreement between water depths estimated by (non-linear) depth inversion and the observations. He arrived at values of $f(m) = 0.42$ and 0.48 depending at which cross-shore location wave heights (also an input to Eq. (7)) were measured. Bell et al. (2004) simply assumed a value $f(m) = 0.4$ and used the significant wave height measured by an offshore buoy. It is important to note that in these cases, non-linearity is included by means of a non-local value of wave height, i.e. Eq. (7) is used with spatially constant values of $f(m)$ and H . In practice, this simplification is not strictly necessary, nor are the criteria for selecting these values clear.

It is also of note that cnoidal wave theory is asymptotic to linear shallow water (periodic) wave theory as $m \rightarrow 0$ ($Ur \rightarrow 0$) and to the solitary (aperiodic) wave solution as $m \rightarrow 1$ ($Ur \rightarrow \infty$, $f(m) \rightarrow 1$). The solitary wave is a constant form solution often used to describe non-linear behavior in shallow water. In this case the phase speed is given by

$$c = \sqrt{gh(1 + H/h)}, \quad (8)$$

which represents the upper bound on the cnoidal wave phase speed. Some field observations have suggested that nearshore wave speeds are bounded by this limit (Inman et al., 1971; Thornton and Guza, 1982); although, in a few cases the limit has also been exceeded (Suhayda and Pettigrew, 1977; Lippmann and Holman, 1991; Puleo et al., 2003). In general, there is significant variability between the observed phase speeds and the theoretical predictions. One source of this variability is that in these comparisons H/h is generally taken as a global constant, based on the assumption of depth-limited, breaking waves. In this case a typical global value in the field would be $H/h = 0.42$ – 0.43 (e.g. Thornton and Guza, 1983), although observations indicate it can vary spatially between $0.33 \leq H/h \leq 1.1$.

Suhayda and Pettigrew (1977) compared crest speeds measured using photographic methods with Eq. (8). In their work they used the measured local values of H/h and found good agreement with Eq. (8) outside the surf zone, but inside the surf zone measured speeds were found to deviate up to $\pm 20\%$, often exceeding it. We note however, that their use of the still water depth as datum for the wave height measurement (as opposed to the trough depth) would tend to underestimate the modeled speeds somewhat.

2.2. Models for breaking waves

The models described in the previous section were formally derived for non-breaking waves only. In the surf zone, a phase speed model for breaking waves is perhaps more appropriate. A general expression can be obtained for broken waves in the inner surf zone where waves can be considered bores, which are propagating hydraulic jumps whose speed, c_{hj} , relative to a fixed reference frame is (e.g. Abbot and Minns, 1992)

$$c_{hj}^2 = g \frac{d_c (d_t + d_c)}{d_t} \quad (9)$$

where d_t , d_c are the instantaneous water depths at the preceding trough and the following crest, respectively (see Fig. 1). In deriving Eq. (9) it has been assumed that the shallow water assumptions hold, that is, the flow is vertically uniform, pressure is hydrostatic and the bottom is horizontal. Svendsen et al. (1978) derived a more general expression including vertically non-uniform velocity and pressure profiles. However, when both quantities are assumed to be vertically uniform, their expression takes the form

$$\frac{c_b^2}{gh} = \frac{d_c d_t (d_t + d_c)}{h^3} \quad (10)$$

Eq. (10) is slightly different from Eq. (9) because Eq. (9) assumes a bore propagating into quiescent water, whereas if we have a series of waves they will encounter an opposing flow of speed u_t resulting from the orbital motion in the previous wave trough, something that is taken into consideration in deriving Eq. (10). However, it is possible to obtain Eq. (10) from Eq. (9) by using the Galilean transformation $c_b - u_t = c_{hj}$ and a shallow water relation $u_t = c_b \eta_t / d_t$ (Svendsen et al., 2003), η_t being here the local free surface elevation in the preceding trough. Additionally, if $d_c \approx d_t \approx h$, Eqs. (9) and (10) reduce to the linear shallow water approximation.

Svendsen et al. (1978) and Stive (1984) found good agreement between Eq. (10) and their experimental data for laboratory regular waves on planar beaches; Buhr Hansen and Svendsen (1986) found similar results in the laboratory but on the seaward side of a nearshore bar. It is of note that all of these previous experiments were run on relatively mild slopes ($\beta \leq 1:34$) and with a limited range of water depths ($kh_{\max} = 0.46$). Stive (1984) also introduced a phase speed correction to account for non-uniformities in the velocity profile due to the presence of turbulence. His results showed a slightly improved agreement as compared to Eq. (10); however, they

required detailed knowledge of the velocity profile at each section, which makes the method difficult to apply.

It can also be shown that Eqs. (9) and (10) collapse to the same value if $d_t = h$, which corresponds physically to the case of a single bore propagating into quiescent water. If the instantaneous water depth at the crest is defined as $d_c = h + H$ where H is taken as the height of the bore, Eq. (10) can also be written as

$$\frac{c_b^2}{gh} = 1 + \frac{3H}{2h} + \frac{1}{2} \left(\frac{H}{h} \right)^2 \quad (11)$$

which predicts speeds slightly larger than solitary wave theory. The first two terms on the right-hand side of Eq. (11) were also considered by Suhayda and Pettigrew (1977), and they showed good agreement to this model in the area near the onset of breaking where the observed crest speeds exceeded solitary wave theory by $\sim 20\%$.

An empirical alternative arises from observations showing that the phase speed in the surf zone is slightly larger than the linear approximation but still typically proportional to $h^{1/2}$ (Svendsen et al., 1978). Thus, a simple approach is to model phase speeds with a modified shallow water approximation

$$c = a \sqrt{gh} \quad (12)$$

where a is a constant to be determined. This approach has been used in various wave models owing to its simplicity, with a typical value of $a = 1.3$ (Schäffer et al., 1993; Madsen et al., 1997a). This value is consistent with the surf zone observations of Stive (1980), which considered regular laboratory waves. This value is also consistent with the solitary wave solution (Eq. (8)) using a global value of $H/h = 0.78$. Eq. (11) can also be reduced to the form of Eq. (12) if a global $H/h = 0.42$ is assumed in the surf zone, which leads to $a = 1.31$. Stansby and Feng (2005) presented phase speed data from one laboratory condition (regular wave) and their results showed a monotonic cross-shore variation for the proportionality constant in the range $a = 1.06$ – 1.32 .

Recently, Bonneton (2004) developed a celerity model using Saint-Venant shock wave theory in which the roller height can be different from the wave height. The resulting expression for the bore speed is

$$c = -2\sqrt{gh_m} + 2\sqrt{gh_t} + \sqrt{\left(g \frac{h_c}{h_t} \left(\frac{h_t + h_c}{2} \right) \right)} \quad (13)$$

where h_m , h_c , h_t are the mean, crest, and bore toe levels, respectively. If we set $h_m = h_t = d_t$ and $h_c = d_c$, the model collapses to Eq. (9); hence, the effect of the returning flow has been neglected. This model showed relatively good agreement when compared to the experimental data of Stive (1984) and Buhr Hansen and Svendsen (1979). In some cases it represented an improvement over the bore model (Eq. (10)) and the simple model given by Eq. (12).

2.3. Composite models

Non-linear effects can be of importance in the intermediate depths ($\pi/10 < kh < \pi$) of the shoaling region as well, which also

includes the transition from non-breaking to breaking waves. Therefore, some composite models have been introduced that attempt to span this range of conditions.

For example, Svendsen and Buhr Hansen (1976) found that a combined linear-cnoidal model performed well for waves with a small deep water steepness, H_o/L_o . In this approach, linear theory is used for $h/L_o > 3/8\pi$, and cnoidal theory otherwise. However, forcing the wave heights to match at the matching point between the two theories causes a discontinuity in the energy flux. Also, if the deep water steepness is greater than 4%, a higher-order Stokes model should be used instead of linear theory. In turn, Flick et al. (1981) found that non-linear shoaling effects can be well described by third-order Stokes theory as long as the Ursell number remains $O(1)$ or less. Furthermore, Stokes theory provided the same functional form in terms of Ur as cnoidal theory when $kh \ll 1$ and $Ur \ll 1$, which allows both models to be coupled. Svendsen et al. (2003) used cnoidal theory up to the break point and the bore model given by Eq. (10) in the inner surf zone. The phase speed in the outer surf zone was interpolated between these end values and was generally in good agreement with the regular wave lab data of Buhr Hansen and Svendsen (1979) and Svendsen and Veeramony (2001).

However, one shortcoming of these combined models is that they require an explicit determination of the coupling boundary. An alternative is to find a unique mathematical expression that can be used over a wider range of conditions and in a more predictive sense, with no a priori analysis of the wave conditions required to link the various phase speed models.

Hedges (1976) used solitary wave theory as a reference to modify the linear dispersion equation to include non-linear effects by explicitly including wave height

$$c^2 = \frac{g}{k} \tanh(k(h + Z)), \quad (14)$$

where $Z=H$. Booij (1981) compared Eq. (14) with the shallow water data of Walker (1976) and found that $Z=H/2$ provided a better agreement. Kirby and Dalrymple (1986) extended the model of Hedges (1976) so that it could be used over a wider range of relative water depths, but employed $Z=H/2$. In this model, the phase speed is given by

$$c^2 = g/k(1 + f_1\epsilon^2 D) \tanh(kh + f_2\epsilon), \quad (15)$$

where $\epsilon = kA = kH/2$, $A=H/2$ is the wave amplitude and

$$D = \frac{8 + \cosh 4kh - 2 \tanh^2 kh}{8 \sinh^4 kh}, \quad (16)$$

$$f_1(kh) = \tanh^5(kh), \quad f_2(kh) = \left(\frac{kh}{\sinh(kh)} \right)^4. \quad (17)$$

This model collapses to linear wave theory when $A \rightarrow 0$. The model (henceforth KD86) is asymptotic to third order Stokes theory in deep water, where $D \rightarrow 1$, $f_1 \rightarrow 1$ and $f_2 \rightarrow 0$. In shallow water, where $f_1 \rightarrow 0$ and $f_2 \rightarrow 1$, the model is asymptotic to Eq. (14) with $Z=H/2$.

2.4. Summary

Up to this point, we have summarized a number of formulations previously used for estimating the phase speed of waves in (or near) the surf zone. In the remainder of this paper, we will investigate the performance of many of these models against experimental remote sensing data. The models to be studied are listed in Table 2 in Section 4.2, and include both breaking and non-breaking wave models and models that have been used in previous depth inversion algorithms.

3. Experiment description

Large scale laboratory experiments were performed in the Large Wave Flume (LWF) at the O.H. Hinsdale Wave Research Laboratory (Oregon State University). The usable length of this flume is approximately 90 m, and it is 3.7 m wide and 4.6 m deep. The flume has a flap-type wavemaker at one end. The LWF coordinate system has the x -axis pointing onshore along the centerline with the origin at the wavemaker, and where water depth was 4.27 m. A piecewise linear bathymetric profile was constructed by using 12 ft long concrete slabs mounted on brackets upon the tank walls. Gaps between slabs were sealed using aluminum plates. The profile was designed to approximate the bar geometry of an observed field beach at a 1:3 reduction in scale (see Scott et al., 2005). The final bathymetry was surveyed using a total station, which provided enough vertical precision to resolve the minor deflection at the slab centers due to their own weight as seen in Fig. 2.

3.1. Wave conditions

Six resistance-type wave gages were used to measure free surface elevation and were sampled at 50 Hz. The wave gages were installed on the east wall of the tank at cross-shore locations $x=23.45, 45.40, 52.73, 60.04, 70.99$ and 81.97 m as shown in Fig. 2. For the present work, six regular wave conditions were tested and are listed in Table 1. Two independent runs were performed for each condition and showed a high level of repeatability. The given breaking wave height values correspond to the largest wave height measured for a given condition. The Iribarren number $\xi_b = \beta/\sqrt{H_b/L_o}$ at the break point was computed with a representative slope $\beta=1/24$, corresponding to the offshore face of the bar where waves began to break for the majority of the cases. The Iribarren numbers indicate that the breaking regime was spilling ($\xi_b < 0.4$) to plunging ($0.4 < \xi_b < 2.0$) (Komar, 1998). Further details of the experimental procedure can be found in Catalán (2005) and Catalán and Haller (2005).

3.2. Video data

Simultaneous video observations were collected using an ARGUS III video station. This station is maintained by the Coastal Imaging Lab (College of Oceanic and Atmospheric Sciences, OSU) and consists of three digital cameras mounted near the laboratory ceiling and aimed at different sections of the

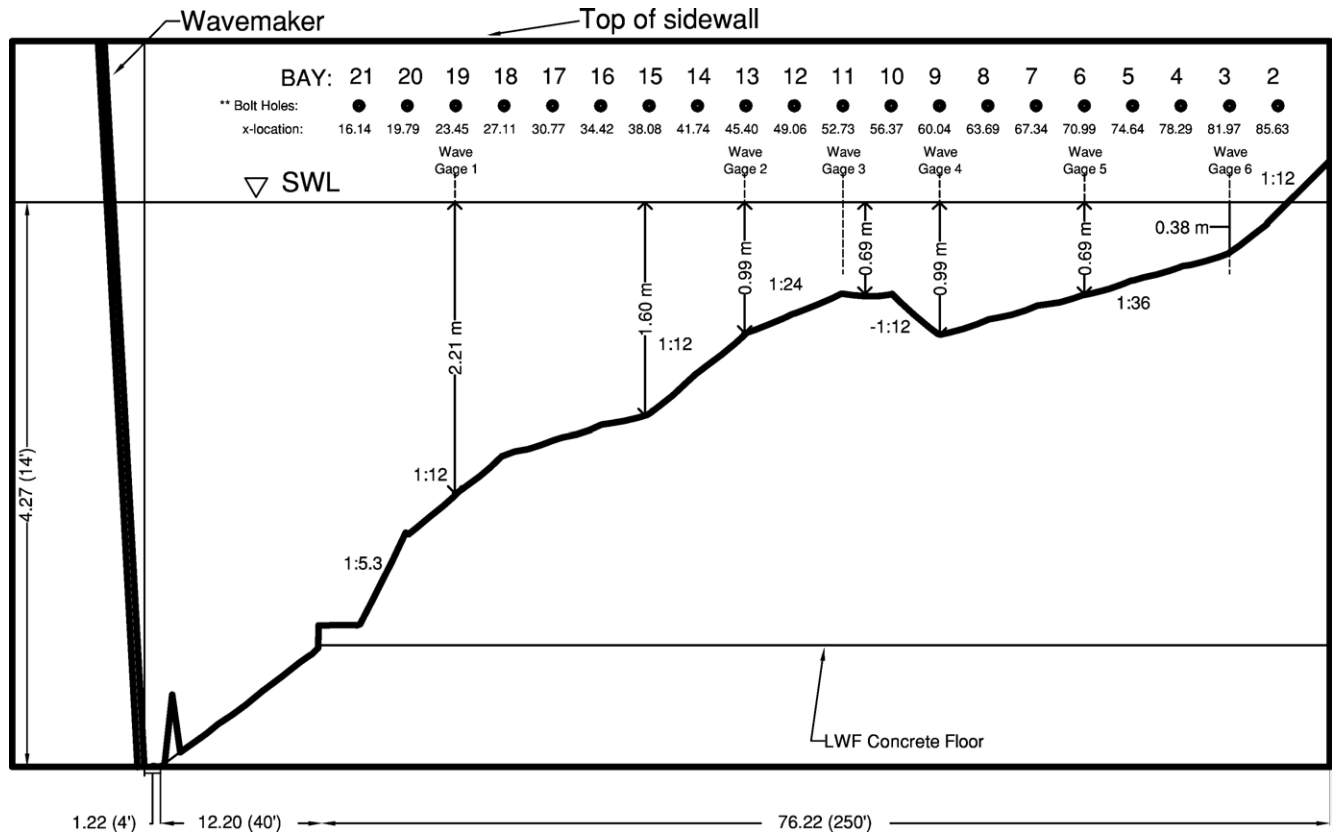


Fig. 2. Experimental layout for the Large Wave Flume, including bathymetric profile, wave gage locations, and bay numbering scheme.

LWF. The cameras are 9.88 m above the still water level in the LWF and the field of view of the cameras spans the cross-shore from $x=41.7$ m to the dry beach.

Three different pixel arrays were sampled at 10 Hz, spanning $41.7 < x < 100$ m at longshore coordinates $y=1.2$, 0 and -0.6 m. Actual camera resolution varies from $1 \text{ cm}^2/\text{pixel}$ close to the cameras ($x=52.73$ m) to $8 \text{ cm}^2/\text{pixel}$ near the shoreline. After interpolation to a uniform grid, there were a total of 5736 pixels in each array with a resolution $\Delta x=1$ cm. However, the effective resolution depends on the sampling rate and the local speed of the wave motion, which meant that some of the data were statistically redundant; therefore, they were subsampled to a resolution of $\Delta x=25$ cm. The resulting resolution per incident wavelength, $\Delta x/L$, was 0.02 on average for these experiments. This is significantly better than most field situations (e.g. $\Delta x/L \approx 0.06$ for Stockdon and Holman (2000)). Wave conditions in the tank were essentially uniform in the y -direction (long-shore); however, the lighting conditions were not. We restricted our analysis to the pixel array (at $y=1.2$ m) that was least degraded by the ambient lighting conditions. In the end, the data products that were used for this analysis were time–space maps of pixel intensity, also known as timestacks, generated from the pixel array. Further details of the video data processing can be found in Catalán (2005).

Pixel intensity is related to water surface elevation through a modulation transfer function (MTF) that governs the relationship between phases and amplitudes of the observed signal and the true waveform. The MTF will depend on the mechanism by

which the waves are imaged by the camera. When waves are not breaking, the principal mechanism is specular reflection of the incident light on the free surface. This specular reflection depends on the instantaneous angle defined by the light source, the water surface, and the camera, and also the relative angle between the direction of wave propagation and the camera. However, regions where the surface slope changes rapidly can induce brightness variations not necessarily related with the true wave signal, which can hinder its identification.

These issues associated with specular reflection are not as important in regions where waves are breaking, in which case isotropic scattering from the aerated and turbulent region of the wave roller is the main observational mechanism (Stockdon and Holman, 2000), and there is relatively little dependency on the viewing geometry. However, the signal from persistent foam

Table 1

Wave conditions: Wave period T , deep water wave height H_o , deep water steepness H_o/L_o , breaking wave height H_b , relative water depth at break point $(kh)_b$, Iribarren number ξ_b , and Ursell number Ur_b at the break point

Run	T (s)	H_o (m)	$\frac{H_o}{L_o}$	H_b (m)	$(kh)_b$	ξ_b	Ur_b
R35	2.7	0.57	0.050	0.63	0.66	0.18	1.06
R36	4.0	0.63	0.025	0.67	0.43	0.25	2.68
R37	5.0	0.51	0.013	0.78	0.34	0.29	5.00
R38	6.0	0.47	0.008	0.68	0.28	0.38	6.49
R39	8.0	0.37	0.004	0.73	0.21	0.49	12.40
R40	4.0	0.40	0.016	0.55	0.43	0.28	2.21

may also need to be removed (e.g. Aarninkhof and Ruessink, 2004) in order to correctly isolate the propagating wave signal.

In order to avoid the problems associated with specular reflection in the laboratory (where we have distinct, non-diffuse light sources), we have focused on the much clearer signal from the breaking wave roller. This, by definition, limits our analysis to the surf zone (but not necessarily shallow water).

3.3. Phase speed measurement

Validation of the aforementioned models requires comparisons to observations; however, the existing literature demonstrates that phase speeds are extracted from observations in a number of different ways depending on the nature of the data set. For instance, for experimental data using regular waves, phase speed is typically defined as the mean velocity of propagation of a characteristic wave point traveling between two cross-shore locations. Thus, if the distance between the two locations is Δx and the tracking time is Δt , then the phase speed is $c = \Delta x / \Delta t$. The wave front, $\eta = 0$, is often chosen as the characteristic point (e.g. Svendsen et al., 1978), although Stive (1980) showed that, for waves in the inner surf zone, the velocities of crest, front and troughs were all similar. Clearly, for phase speed measurements based on the travel time between two points, a high-resolution array of sensors (in-situ) or of pixels (remote sensing) is needed to estimate local phase speeds. Else, measured speeds will represent an average speed across a variable depth profile.

Estimation of phase speed from this data set is performed using the tracking technique applied to the toe of the roller, owing to its relatively simple identification from the pixel intensity signal. This can be seen in Fig. 3b where the roller toes (or roller fronts) are characterized by a large increase in a given pixel intensity time series $I(x', t)$. These fronts can be identified by zero-up crossings of a threshold pixel intensity value chosen here as $\bar{I} + \sigma_I$, where \bar{I} , σ_I are the mean and standard deviation of the pixel intensity of a given timestack $I(x, t)$. Identification of these fronts shows little sensitivity to the threshold value due to the strong gradients in $I(x, t)$ near the roller front. It is also evident in Fig. 3 that the intensity values are clipped at a value of 220 (as opposed to 255), which is a result of the procedure used to merge images from different cameras. This has no effect on the phase speed estimation.

At times, trajectory tracking techniques can lead to noisy phase speed profiles. More stable statistical estimates can be obtained when the result is averaged over several waves, making this technique most suitable for regular wave conditions. For the present case, we average over all waves present in an experimental run (> 50 waves) and also average together two experimental runs with the same input wave conditions. Finally, some spatial smoothing was performed by using a running average with a 2.5 m window.

Other measurement techniques were also tested including spectral methods and CEOF analysis. However, for the regular conditions analyzed herein these methods led to phase speed profiles that showed significant modulations shoreward of the bar. Grilli and Skourup (1998) found similar behavior in a

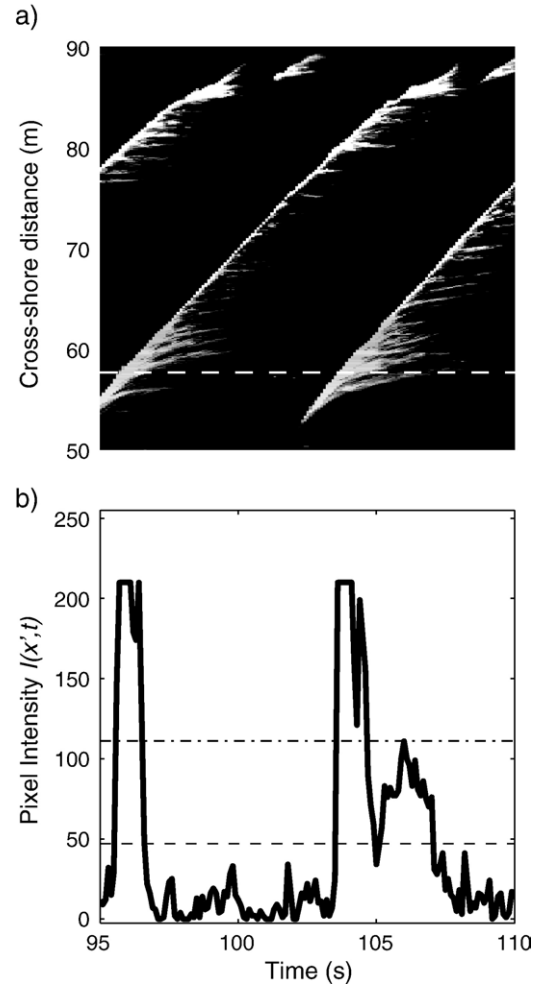


Fig. 3. Example video data from Run 39; a) timestack $I(x, t)$ with horizontal dashed line indicating cross-shore location $x' = 58$ m.; b) pixel intensity time series $I(x' = 58 \text{ m}, t)$. Dashed line is the value of mean intensity, \bar{I} , dash-dotted line is $\bar{I} + \sigma_I$ and is used to identify the breaking wave fronts.

numerical study of regular waves over a barred profile, an attributed it to free harmonics being released on the shoreward face of the bar, which modulated the fundamental wave component. The resulting phase speed profiles exhibited shorter scale variations that were not correlated with the bathymetric profile, thus limiting their applicability to depth inversions. For these reasons such methods are not considered in the remainder of this paper.

4. Results

4.1. Observed phase speeds

Fig. 4 shows phase speed profiles derived from the front-tracking algorithm for all the runs. Several regions can be identified in this figure. Offshore of the bar, the absence of wave breaking prevents the use of the front-tracking technique, thus yielding no speed values. Shoreward of this region a narrow region exists where the observed speeds show a large increase as the waves began to break (typically around $x = 52$ m). These

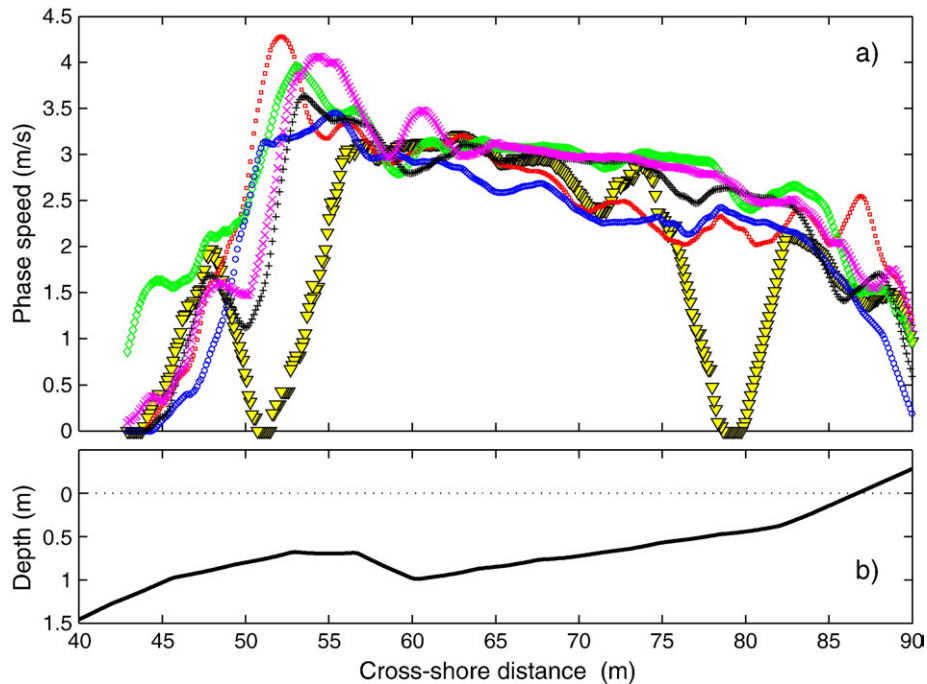


Fig. 4. Video phase speed profiles for Run 35 (blue ○), Run 36 (red □), Run 37 (magenta ×), Run 38 (green ◇), Run 39 (black +) and Run 40 (yellow ▽). b) Bathymetric profile.

speeds seem to show no visual correlation with bathymetric features. Similar results were given by Svendsen et al. (2003), who found speeds more than two times the local value of \sqrt{gh} in the outer surf zone. The increased phase speeds observed in the outer surf zone are likely the result of the process of wave roller formation (see e.g. Basco (1985) for a description).

The region spanning the bar trough to the shoreline can be considered the inner surf zone, and here the observed speed profile is relatively smooth, although some oscillations are present. Finally, there is a third region near the still water shoreline where the observed velocities are still non-zero due to the non-zero water depths resulting from the wave setup. In this region some cases exhibit another increase in phase speed, which is attributed to a second breaker line at the shoreline, which can be seen in Fig. 3 near $x=87$ m, $t=100$ s. Finally, it can be seen in Fig. 4 that Run 40 exhibits a region of zero observed velocities that is a result of the cessation of breaking near $x=80$ m; this case will not be considered in the subsequent analysis. In addition, the same tracking technique was applied to the wave gage data from the long period case (R39) for comparison. The values thus obtained represent an average of the wave speed between the gages used in the analysis, and show an excellent agreement with the video observed speeds, as can be seen in Fig. 6c.

4.2. Modeled phase speeds

The observed speeds are compared with those obtained using the phase speed models listed in Table 2. Many of the phase speed models reviewed introduce non-linearity through the local wave height, while some of them need estimates of the

local water depth under the crests and troughs as well. However, the remote sensing data from these experiments only provides high-resolution phase speeds, not wave heights or water depths. It should be noted that there do exist some remote sensing technologies that are capable of measuring wave heights (e.g. Dankert and Rosenthal, 2004; Izquierdo et al., 2005), but their application to the nearshore has not yet been demonstrated. However, it is reasonable to expect remotely sensed wave heights to be available at the appropriate resolution in the future. Nonetheless, at present these quantities need to be measured by in-situ gages. In order to match the in-situ resolution with the remote sensing resolution, the profiles of wave height (H), wave setup ($\bar{\eta}$) and crest and trough depths (d_c , d_t) were linearly interpolated between the six wave gages. Fig. 5 shows an example of the interpolated quantities. Additionally, wave height and wave setup were linearly extrapolated to the still water shoreline; wave height was set to zero at the shoreline. For the shock model of Bonneton (2004), it is assumed that the bore front is located near the mean water level, hence $h_t = h_m$ in Eq. (13). This was found to be a reasonable assumption based on an examination of synchronized and co-located video and wave gage data. It is also stressed that for all comparisons with the solitary wave model, the value of H/h is calculated at each cross-shore location. For the case of the modified cnoidal equation, we used a fixed value of $f(m)=0.4$ as in Bell et al. (2004), and we tested three possibilities for the input wave height H^* : the local value, the maximum wave height (non-local) and the offshore wave height (non-local).

Figs. 6 and 7 show the resulting phase speed profiles and phase speed ratio C_m/C_{obs} for a selected subset of the models in Table 2. These models were chosen because of their differing

Table 2

Table of phase speed models used in the analysis; percent relative error of the phase speed models in the region $60.04 \leq x \leq 81.97$ m, \bar{R}^c mean relative error and \bar{R}_{RMS}^c average root-mean-square error

Model	Equation	\bar{R}^c	\bar{R}_{RMS}^c
Linear theory	$c^2 = \frac{g}{k} \tanh(kh)$	-7.4	10.5
Solitary	$c = \sqrt{gh \left(1 + \frac{H}{h}\right)}$	17.9	19.2
Modified shallow	$c = 1.3 \sqrt{gh}$	24.0	25.7
Cnoidal theory	$c = \sqrt{gh \left[1 + \frac{H}{mh} \left(2 - m - 3\frac{E}{K}\right)\right]}$	7.0	9.1
Modified cnoidal	$c = \sqrt{gh(1 + f(m)H^*/h)}$		
	$H^* = H_{\text{local}}$	5.0	10.1
	$H^* = H_{\text{max}}$	13.3	14.7
Bore	$H^* = H_{\text{off}}$	9.1	11.9
	$c_b^2 = gh \frac{d_t}{h^3} \left(\frac{d_t + d_c}{2}\right)$	13.3	14.7
Shock	$c = -2\sqrt{gh_m} + 2\sqrt{gh_t} + \sqrt{\left(g \frac{h_c}{h_t} \left(\frac{h_t + h_c}{2}\right)\right)}$	24.1	25.1
KD86	$c^2 = g/k(1 + f_1 \epsilon^2 D) \tanh(kh + f_2 \epsilon)$	2.8	8.0
Hedges	$c^2 = \frac{g}{k} \tanh(k(h + H))$	11.1	12.7
Booij	$c^2 = \frac{g}{k} \tanh(k(h + H/2))$	2.7	8.0

degrees of non-linearity (cnoidal, solitary, KD86), their previous application in depth inversion studies (linear) and their inherent basis on surf zone breaking waves (bore). It was found that the modified shallow water and the shock model overpredicted the speed significantly irrespective of the wave conditions. In addition, the models of Hedges (1976) and Booij (1981) exhibit a very similar trend to that of the KD86 model. For these reasons they are not included in the figure, whilst they remain in the overall analysis.

Figs. 6 and 7 show three of the five conditions tested; the most and least dispersive (R35 and R39, respectively), and the condition with the largest non-linearity (R37). The models exhibit piecewise linear phase speed profiles, which is attributed to their direct dependency on the water depth. The magnitudes of the observed speeds over the bar are bounded by the solitary and linear models, consistent with previous findings. However, it is not immediately obvious which model provides the best agreement. In addition, discrepancies are significant over the bar at the onset of breaking, where the direct dependency on the water depth makes almost all models predict decelerations followed by accelerations at the down slope on the shoreward side of the bar, whereas the observed speeds show exactly the opposite trend. The results for the shock model suggest it does relatively better in this region (not shown), but a more conclusive analysis would require higher resolution in the narrow region over the bar.

In the region shoreward of the bar trough ($60 < x < 82$ m), all models are in agreement with the observed trend of steadily decreasing speeds consistent with a linear bathymetric profile. Overall, the linear model appears to do best at higher relative water depths, kh , i.e. for shorter periods and larger depths. However, as waves enter shallower water the observed speed gradually approaches the KD86 model or cnoidal models, and eventually the bore model. The asymptotic behavior of the composite model to that of Booij (1981) means they are almost indistinguishable for most of the domain.

Agreement typically deteriorates in the region between $x = 85$ m and the still water shoreline at $x = 86.65$, where all the models predict a sharp decay in phase speeds. All models fail to predict the observed speeds shoreward of the still water shoreline. In some cases, a large increase in the speed occurs that can be associated with a secondary breaker that is being picked up by the tracking algorithm.

It is of interest to compare the performance of the speed models in the region where all relevant parameters can be

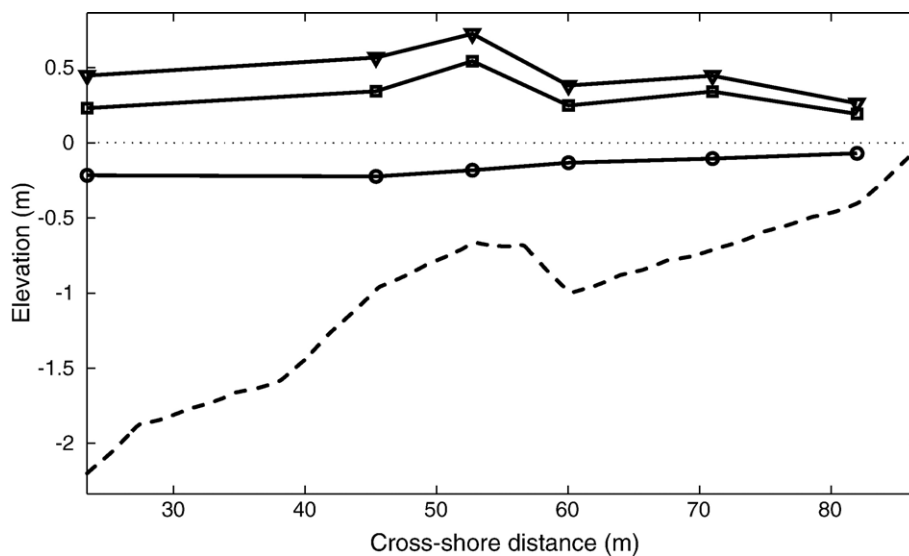


Fig. 5. Example of interpolated in-situ data, Run 39. Wave height H (∇); (\square) mean crest elevation d_c ; mean trough elevation d_t (\circ) and bathymetric profile (black - - -).

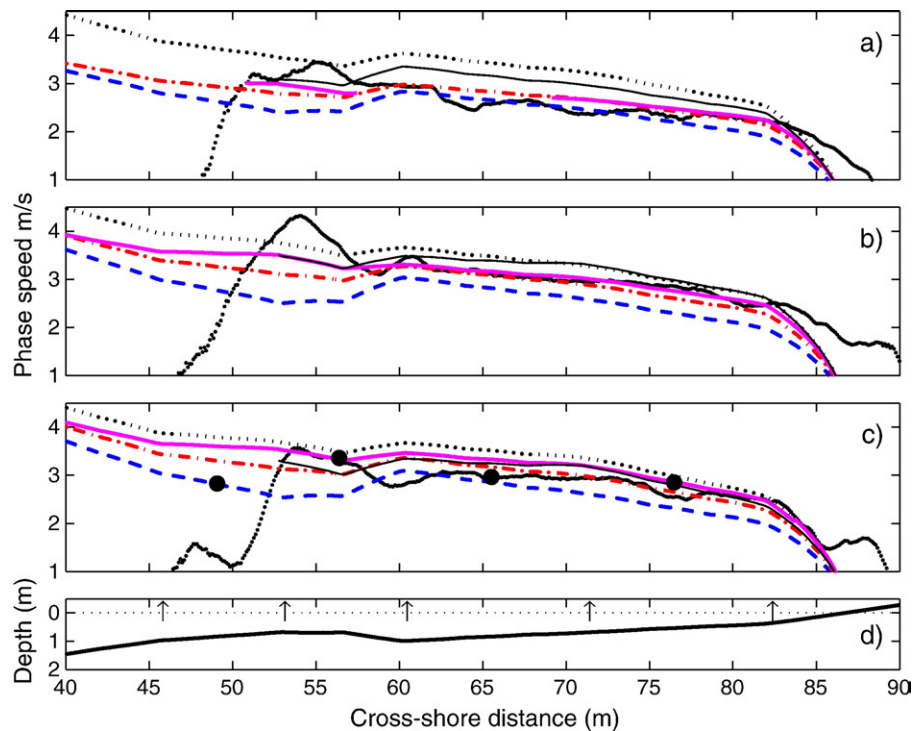


Fig. 6. Comparison between modeled and observed phase speeds, a) Run 35 ($H=0.6$ m, $T=4.0$ s), b) Run 37 ($H=0.5$ m, $T=6.0$ s), c) Run 39 ($H=0.4$ m, $T=8.0$ s), d) Bathymetry. Observed (dots); linear theory (dashed thick blue); solitary (solid dotted black); cnoidal (solid magenta); KD86 (dash-dot thick red); bore (solid thin black); In-situ speeds denoted by (\bullet), up arrows denote the location of in-situ gages.

assumed known. For this reason, we focus our attention on the region spanning from $x=60.04$ m (the bar trough) to $x=81.97$ m. Two criteria governed this choice. First, the physical processes taking place over the bar crest (onset of

breaking) are not well described by any of the models under study. Second, model results beyond $x=81.97$ m rely on the extrapolated wave setup information. Both effects add an unquantifiable source of error that could mask the true

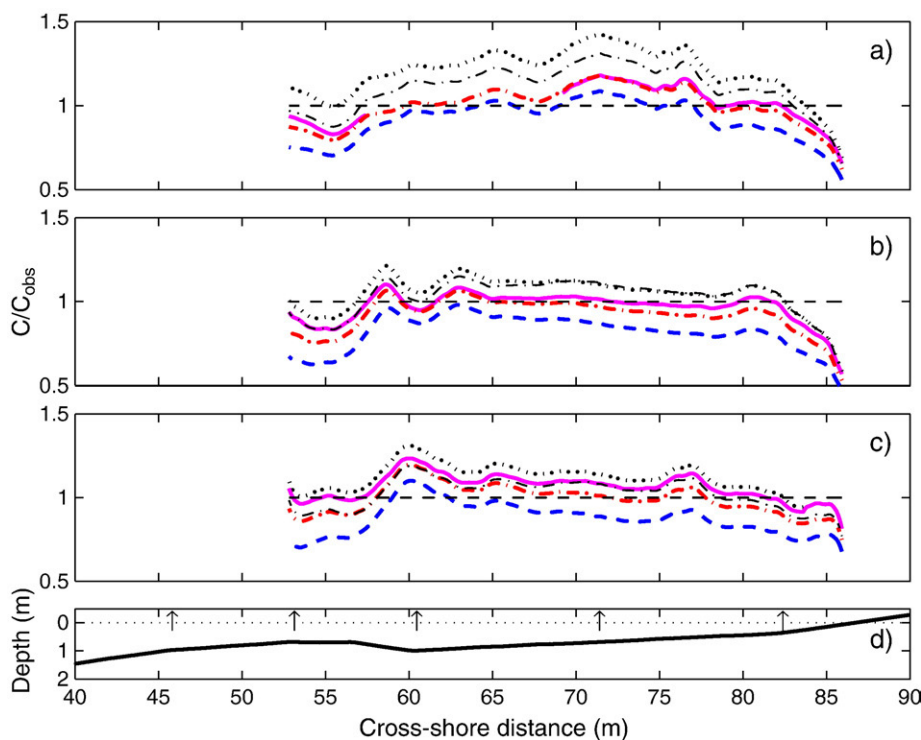


Fig. 7. Ratio between modeled and observed speeds, C_m/C_{obs} . Same color coding as Fig. 6.

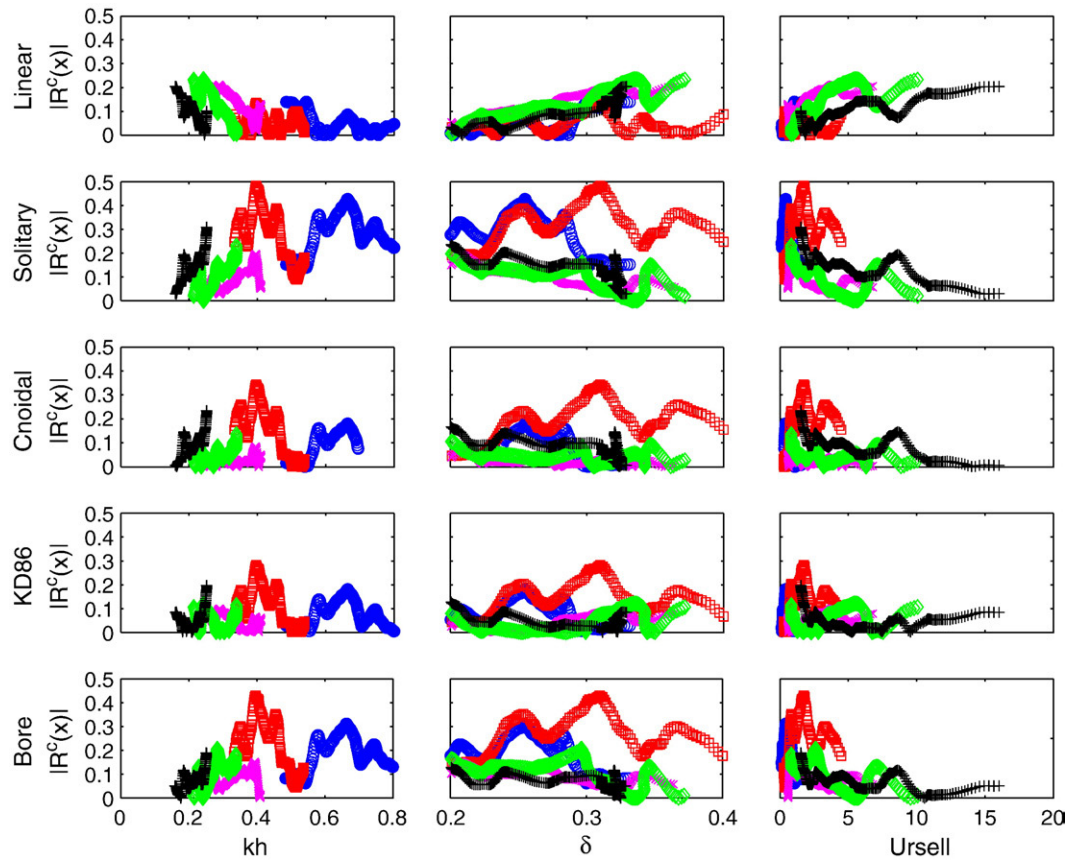


Fig. 8. Distribution of the absolute relative error $|R^c(x)|$ against dispersiveness $\mu = kh$, non-linearity δ and Ursell number, for each model tested. Run 35 (blue \circ); Run 36 (red \square); Run 37 (magenta \times); Run 38 (green \diamond) and Run 39 (black $+$).

performance of the models in their region of applicability. For the analysis we use cross-shore profiles of the absolute relative error defined as

$$R^c(x) = \frac{c_{\text{model}}(x) - c_{\text{obs}}(x)}{c_{\text{obs}}(x)}, \quad (18)$$

where c_{model} , c_{obs} are the modeled and observed phase speeds, respectively.

Considering the possible dependency of this error on the dispersiveness μ and non-linearity δ , each local estimate of the relative error is plotted against these parameters for the selected models in Fig. 8. Here the absolute value $|R^c(x)|$ is shown in order

to simplify the analysis. It should be mentioned that for the waves of smallest period (R 35), the limit of applicability for the cnoidal model ($h/L_o < 3/8\pi$) is breached at some locations. These points were removed from the data set of that particular run and no attempts were made to combine it with another model.

Dispersiveness is computed based on the local wavenumber from linear theory and ranges from $0.15 < kh < 0.81$ for these tests, which corresponds to shallow to intermediate water conditions. Fig. 8 confirms that the linear model performs better where dispersiveness dominates but has large errors in shallow water. The relative error also increases, as expected, with non-linearity. Both effects are combined in the Ursell number, in which case linear wave theory performs well when non-linearity is less than or equal

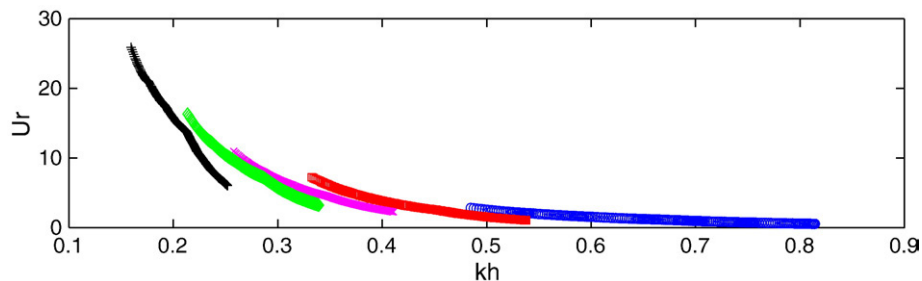


Fig. 9. Ursell number as a function of dispersiveness kh for tested wave conditions within the limited cross-shore domain. Run 35 (blue \circ); Run 36 (red \square); Run 37 (magenta \times); Run 38 (green \diamond) and Run 39 (black $+$). (For interpretation of the references to colour in this figure legend, the reader is referred to the web version of this article.)

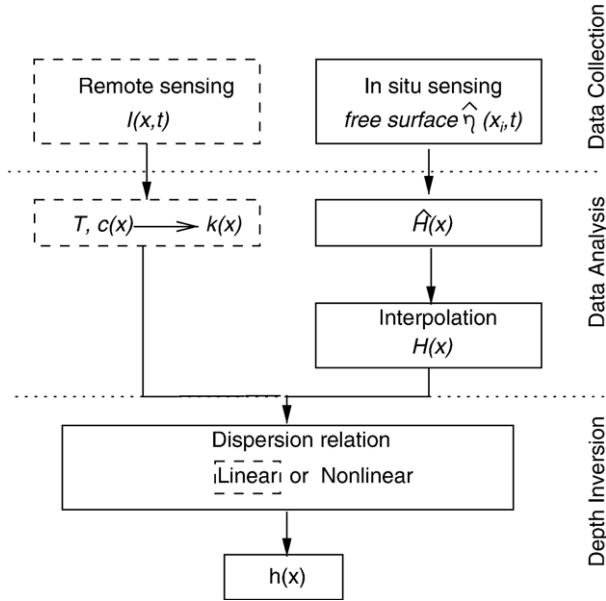


Fig. 10. Flowchart of the inversion algorithm. Dashed lines represent steps for linear inversions, solid lines additional steps for non-linear inversions. For the present implementation, (^) denotes data with low spatial resolution.

to dispersiveness (i.e. $Ur < 1$). The opposite trend is true for the shallow, solitary and shock models, which exhibit the smallest errors at high Ursell numbers, but large errors for the opposite conditions (only solitary model shown). A similar trend was observed with the modified cnoidal model, using local values of wave height, although the errors were smaller. Errors were larger if non-local values of wave height were used instead.

In general, the cnoidal model and all the composite models seem to have relative errors that are somewhat uniformly

distributed across all water depths with a slight increase with non-linearity, which translates into a weak dependency on the Ursell number. Furthermore, the errors are confined in the range $\pm 20\%$ for all values of kh and δ . Finally, the accuracy of the bore model is also dependant on dispersiveness, with the errors increasing with kh or for decreasing Ursell number. However, the bore model performs very well for small kh values, which may explain the good agreement found in previous studies.

In order to derive a single representative error value, we have two choices. The first is to take the cross-shore mean of the absolute relative error profiles, and then average over all wave conditions in order to obtain a single estimate of the error for each model, \bar{R}^c . However, this value is subject to cancellation of values of the same magnitude but different sign. A root-mean-square value is probably a more representative error measure. A second representative error value can be defined from the absolute relative error profiles determined for each model as

$$R_{\text{RMS}}^c = \sqrt{\frac{1}{N} \sum \frac{(c_{\text{model}}(x) - c_{\text{obs}}(x))^2}{c_{\text{obs}}^2(x)}}, \quad (19)$$

where N is the total number of cross-shore locations considered. This calculation provides a R_{RMS}^c estimate for each model and each wave condition, which are then averaged over the wave conditions to obtain a single estimate of the error for each model \bar{R}_{RMS}^c . This error measure represents the average phase speed error when considering a range of incident wave conditions and observation locations.

Columns 3 and 4 in Table 2 list each of the representative error values and show that the composite (KD86 and Booij (1981)) and modified cnoidal models have the smallest errors and are somewhat better than the linear and bore models. The asymptotic nature of the KD86 model to that of Booij (1981) makes the two

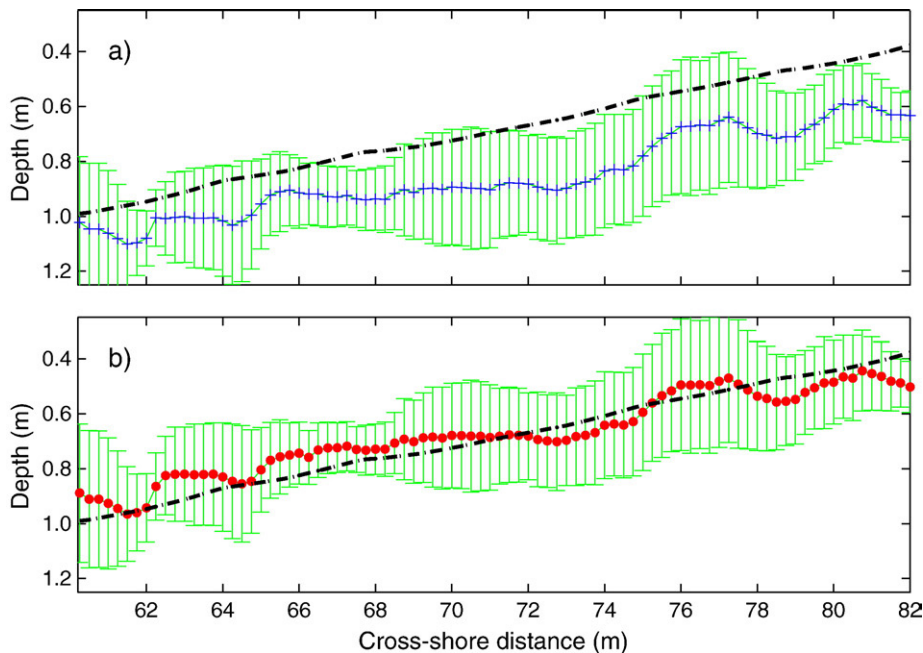


Fig. 11. Estimated median depth profile using a) linear (+); b) KD86 (●) dispersion model. Vertical error bars correspond to 95% confidence level.

hard to distinguish for the present wave conditions and they accordingly yield similar relative error values. The shallow water, solitary, and shock models fair much worse, since the range of water depths considered well exceeds their region of validity. The linear model performs somewhat better than the shallow water models, which appears to result from the fact that Ursell numbers are not very large over a good portion of the domain for the majority of the cases studied (see Fig. 9).

In summary, the Booij (1981) and KD86 model provided the best overall agreement, which indicates the strength of the composite models. The modified cnoidal model that utilized the local wave height measure was next best, and all of these tend to offer good results over the range of Ursell numbers. However, the performance of the modified cnoidal model is clearly dependant on the choice of a characteristic wave height. Although other models may provide better estimates locally under the appropriate conditions, the benefit of providing dispersive and non-linear behavior in a single model makes it the most suitable for non-linear depth inversions. The expected better performance in intermediate to deep water gives the composite models an extended range of applicability and an overall advantage.

4.3. Depth inversions

Up to this point, we have assessed the performance of a range of phase speed models in comparison to experimental data. In the following section, we will quantify the potential benefit of incorporating the locally measured finite amplitude effects into the depth inversion algorithm. Based on our previous results, we will focus on a composite model (KD86), since the composite models performed the best of the non-linear models and we will compare it to simple linear dispersion.

Local wavenumbers are estimated directly as the ratio between the observed phase speed and the radian frequency $\sigma = 2\pi f_p$, where the peak frequency f_p is obtained from the pixel intensity spectra. Wave amplitudes are interpolated from the in-situ data and used in conjunction with wavenumbers to invert the appropriate dispersion relation and calculate the local mean water depth. Inversion of the linear model is explicit

$$h = \frac{1}{2k} \ln \left(\frac{gk + \sigma^2}{gk - \sigma^2} \right), \quad (20)$$

whereas the KD86 model requires an iterative procedure. Fig. 10 shows the flowchart of the inversion algorithm, highlighting the additional steps used in this study to include a local measure of non-linearity.

After subtracting the interpolated wave setup profiles, the resulting bathymetric profiles are compared with the known still water depth. Over the bar, the observed increase in speed would lead to a trench in the depth profiles rather than a bar (see Catalán, 2005; Catalán and Haller, 2005), because as mentioned previously, none of the phase speed models can account for the roller formation process. Hence, in order to not bias the assessment of the inversion algorithms, we again focus on the region shoreward of the bar trough ($x=60.04$ m). Individual bathymetric profiles are obtained for each wave condition, but it is also convenient to

Table 3

Error estimates for individual profiles and the median profile

Case	Linear				KD86			
	\bar{D}	D_{rms}	\bar{R}	R_{rms}	\bar{D}	D_{rms}	\bar{R}	R_{rms}
	m	m	%	%	m	m	%	%
35	0.05	0.10	9.41	19.26	-0.10	0.14	-13.13	20.47
36	0.05	0.11	5.28	14.36	-0.12	0.16	-20.29	27.20
37	0.25	0.26	41.10	44.83	0.08	0.11	14.75	19.85
38	0.23	0.25	39.02	44.89	0.05	0.11	10.93	20.55
39	0.15	0.18	27.15	33.30	-0.03	0.11	-1.39	15.16
Median	0.17	0.18	28.20	31.65	-0.01	0.05	0.94	9.70

Cross-shore mean and rms value of the difference errors (\bar{D} , D_{rms}) and relative errors (\bar{R} , R_{rms}) for each model. Analysis domain contains $60.04 < x < 81.97$ m.

consider the results in terms of a median profile, which is obtained as the median of the individual estimates at each cross-shore location following Stockdon and Holman (2000).

Fig. 11 shows the median profiles determined from each inversion model. Overall, the profile shape is well recovered; vertical error bars correspond to the 95% confidence level. Linear theory typically overpredicts depths, consistent with observed velocities larger than the theoretical value, and agreement seems to deteriorate as water becomes shallower due to increasing non-linearity. The KD86 model for its part underpredicts depths near the bar trough, followed by a region of better agreement.

In order to quantify the agreement, the dimensional difference error $D = h - h_{true}$ (in meters) and the relative error $R = D/h_{true} * 100$ (in %) are computed at each location for each individual wave condition and for the median profile. According to these error definitions, positive values indicate depth overprediction. Cross-shore mean (\bar{D} , \bar{R}) and root-mean-square (D_{rms} , R_{rms}) values of these statistics, calculated for the region $60.04 < x < 81.97$ m, are listed in Table 3. Again the RMS values are probably more representative, since mean values are subject to cancellation.

The results can be summarized as follows:

- Analysis of the individual cases indicates that the non-linear model performs significantly better than the linear as relative water depths decrease (and non-linearity increases).
- Individual profile errors using the non-linear model in the surf zone are of the same order of magnitude as the average errors from previous studies using linear theory in the shoaling zone with small amplitude waves.
- If the median profile is considered, the non-linear model is far superior with the mean relative error \bar{R} reduced from 28% (32% RMS) for the linear model to 0.9% (10% RMS) with the non-linear model.

5. Discussion

5.1. Sources of error

One of the fundamental assumptions of the standard video rectification process is that pixels image the same physical

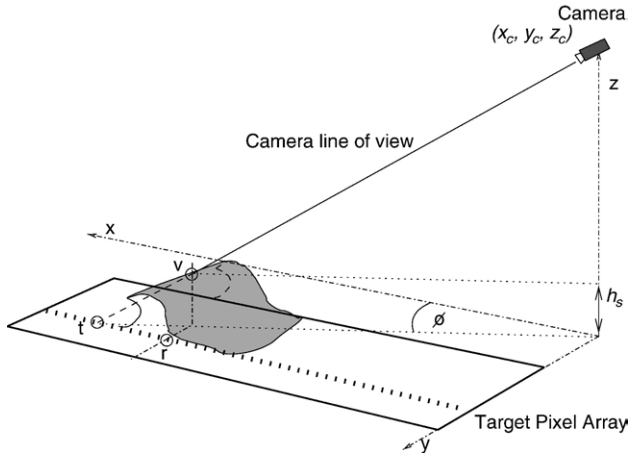


Fig. 12. Misregistration of the pixel array. The target pixel (t) is shadowed by the finite amplitude wave at point (v), which has a corresponding location (r) when projected over the pixel array.

location throughout the collection; thus, the world coordinates of any pixel in the image are known beforehand and remain invariant. Typically for field installations, where the distance to the sea surface is large ($O(100)$ m), it is assumed that the water surface lies on a single horizontal plane (mean sea level), and vertical displacements can be neglected and do not induce artificial horizontal displacements. However, for the present experimental setup, grazing angles were relatively small (about 14° near the shoreline along $y=1.2$ m) and cameras were relatively close to the physical target (the free surface, $O(20)$ m). Vertical displacements in the water surface will lead to video misregistration.

One potential vertical displacement would be the splash-up of a plunging breaker, which may cause the wave front to be associated with a pixel located shoreward of the true front. This isolated, local vertical displacement will translate into a horizontal displacement along the pixel array and lead to a local artificial excess of speed. This effect can be quantified on a geometrical basis, as shown in Fig. 12. A simple estimation shows that the horizontal displacements are equal to $\Delta x = \alpha(x - x_c)$, where x is the cross-shore location of the observed pixel, x_c is the camera location and $\alpha = h_s / (z_c - z)$ is the ratio between the splashing amplitude (h_s) and the vertical distance between the camera and the free surface. For breaking events occurring near $x=54$ m, and with a splashing amplitude of 30 cm, it yields translation errors of $O(5)$ cm. If the splashing event lasts 2 frames ($t=0.2$ s), the spurious velocity will be approximately 0.25 m/s, which represents only a fraction of most of the observed model/data discrepancies, but may be relevant locally. In practice, a rigorous correction for this excess speed is not possible without detailed knowledge of the instantaneous free surface displacement and splashing height.

A second source of vertical displacement is due to finite amplitude waves, and the associated misregistration varies inversely with grazing angle. This type of misregistration results in a more global cross-shore shift in the phase speed profile. The

maximum shift due to this effect is calculated to be about 70 cm and occurs in the vicinity of the still water shoreline (Catalán, 2005). This is expected to have little influence on the results in the present case.

Finally, the existence of mean currents in the surf zone is not accounted for in the phase speed models and may contribute to model/data error. In this laboratory flume undertow would be the main source of any mean current and a rough estimate of the expected undertow velocity was obtained from the experiments of Scott et al. (2005) for a condition similar to R36. For that case the maximum undertow measured over the bar was $\sim 14\%$ of the local linear phase speed, a value slightly larger than 5–8% found by Svendsen et al. (2003) in their experiments.

Considering mean currents in field applications, the effect of longshore currents would likely be negligible based on their quasi-orthogonality with the incident waves. In general, the effect of undertow on phase speeds is likely exaggerated somewhat in 1D laboratory flumes as compared to field situations where mean currents are typically more complex and two-dimensional. However, the presence of rip currents would certainly affect the phase speed locally. Low frequency motions can also change the local value of h over several wave periods, hence affecting the speed of individual waves (e.g. Thornton and Guza, 1982; Madsen et al., 1997b), although the overall effect would average out for long runs (as is the case here).

5.2. Sensitivity of depth inversions to measurement error

It is possible to relate errors in depth retrieval with measurement errors in the input parameters. Using linear theory as the basis for depth inversions, Dalrymple et al. (1998) obtained an analytical expression for the error in the depth estimate showing that the magnitude of the depth error is at least twice the error in the input parameter k or σ , and this factor increases with kh . Hence, phase speed-based depth inversion methods tend to magnify measurement errors.

A similar expression can be obtained for the KD86 model (see Appendix A for details) as given below

$$\frac{\delta h}{h} = \frac{\delta \sigma}{\sigma} F_1(kh, A) - \frac{\delta k}{k} F_2(kh, A) - \frac{\delta A}{A} F_3(kh, A), \quad (21)$$

where $\delta k/k$, $\delta \sigma/\sigma$ and $\delta A/A$ correspond to relative errors (or perturbations) in wavenumber, frequency and wave amplitude. The expected errors in depth estimates using the KD86 model exhibit similar behavior to the linear case in regards to σ and k , but also incorporate a new source of error related to the measurement of wave amplitude, A . The functional dependency of the functions F_1 , F_2 and F_3 on kh and A show that wave amplitude measurement errors do not get amplified as much as those related with k or σ . This is fortunate, and our results from the previous section indicate that even fairly sparse measurements of wave amplitude can be simply interpolated and their inclusion provides an improvement over linear depth inversion methods. For example, if we treat Hedges model as ground

truth, then a depth estimate \hat{h} can be obtained from a measured amplitude A_{meas} as

$$\hat{h} = \frac{c^2}{g} - A_{\text{meas}}, \quad (22)$$

where c is taken as the true phase speed. Hence, the relative error is

$$R = \frac{\hat{h} - h_{\text{true}}}{h_{\text{true}}} = \frac{(c^2/g - A_{\text{meas}}) - (c^2/g - A_{\text{true}})}{h_{\text{true}}} \quad (23)$$

$$= \frac{(A_{\text{true}} - A_{\text{meas}})}{h_{\text{true}}},$$

where A_{true} is the true amplitude. Thus, when linear dispersion is used ($A_{\text{meas}}=0$) the relative error is equal to the non-linearity parameter, $R=A_{\text{true}}/h_{\text{true}}$, which is in accordance with previous observations that correlated depth inversion errors with wave non-linearity (Holland, 2001).

However, even after inclusion of non-linearity, the operational accuracy of phase speed-based depth inversions is governed by the inherent accuracy of phase speed models (and measurements). Under the range of controlled conditions considered here, and with the available high-resolution remote sensing data, the present analysis shows that phase speeds from the KD86 dispersion relation lie within 8% of the measured values. This, in turn, places an effective limit on the vertical size of bathymetric features (i.e. the local depth perturbation) that can be resolved using phase speed depth inversion. In other words, the feature size that can be identified above the “noise” inherent to the model/data agreement.

Considering that under typical field conditions phase speed observations corresponding to a range of wave heights and periods would be available for a given beach morphologic state,

then there will exist some minimum resolvable bottom feature height (vertical amplitude), Δh_{min} , for those conditions. The functional form of Eq. (21) can be used to estimate this minimum height. Under the assumption that errors in phase speed can be attributed to errors in wavenumber, it is possible to estimate the factor F_2 in Eq. (21) as a function of wave period, wave height and unperturbed depth (i.e. expected depth in the absence of the bottom feature). Once the factor F_2 is calculated, the uncertainty region can be determined by

$$\Delta h_{\text{min}} = F_2 * h * \frac{\delta k}{k}, \quad (24)$$

where we choose $\delta k/k=8\%$. For the case of a sand bar with local height Δh_{bar} above the underlying profile, if $\Delta h_{\text{min}} \leq \Delta h_{\text{bar}}$ then the bar would represent a perturbation larger than the underlying uncertainty and should be detected by the method. We also note that this approach implicitly assumes that the waves are in equilibrium with the underlying bathymetry. In fact, this assumption underlies all phase speed models and depth inversion algorithms in general.

In order to study if bottom features typical to field beaches would be detectable by depth inversion algorithms, minimum bar heights as a function of the local unperturbed depth for a range of incident wave conditions were calculated as shown in Fig. 13. The chosen range of wave condition was $T=3.0\text{--}16\text{ s}$ and $H=0.1\text{--}3.0\text{ m}$, with water depths $h=0\text{--}30\text{ m}$. The colored region of the figure represents the range of observable features and indicates that the minimum feature size increases with water depth. The white region in the left side of the figure represents surface piercing bars, which were removed from consideration.

In order to place these results in the context of typical bar sizes and water depths as found in the field, we utilize the

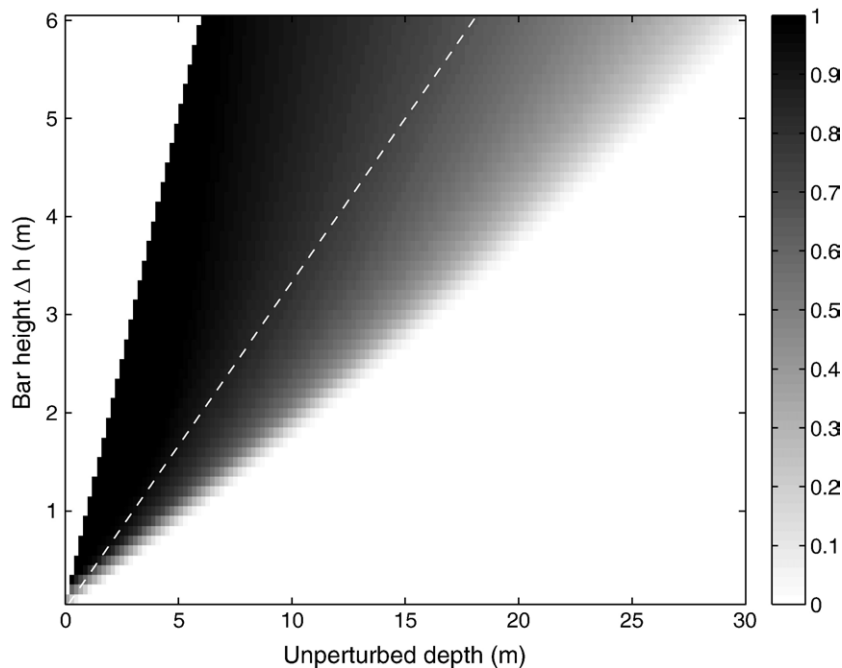


Fig. 13. Fraction of wave conditions in the range $T=3.0\text{--}16\text{ s}$, $H=0.1\text{--}3.0\text{ m}$ capable of detecting a bar. Dashed white line indicates the equilibrium bar height at each depth.

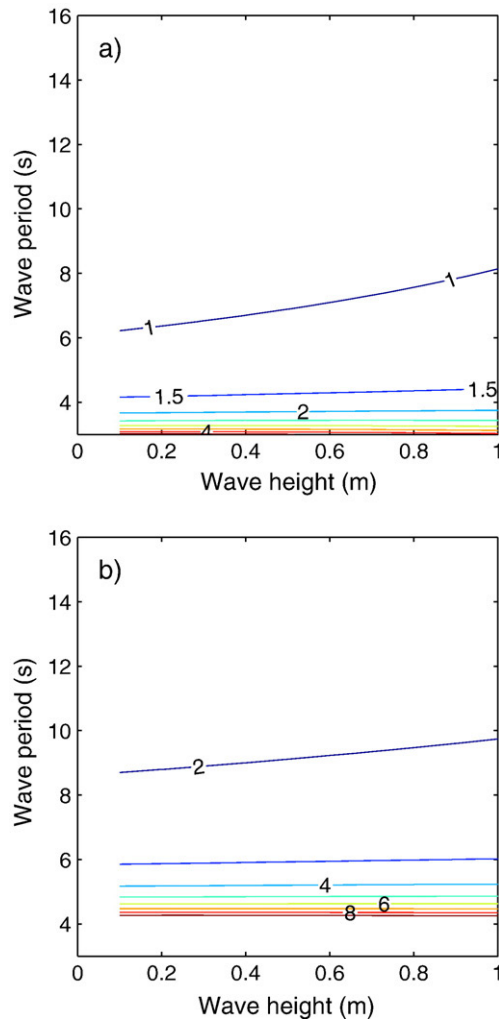


Fig. 14. Minimum identifiable perturbation size (in m) at a given depth, as function of wave height and wave period. a) $h = 5$ m, b) $h = 10$ m.

equilibrium bar profile model of Hsu et al. (2006). Without going into detail, the model provides an analytic, barred profile shape based on given input wave conditions. The model also requires calibration of several empirical coefficients, which we have done here using two barred profiles measured at Duck, NC (see Appendix B). The bar model is used here only to constrain the bar morphologies, which are taken as independent from the expected wave conditions used in the phase speed analysis. The relationship between expected bar heights and depths is shown by the white line in Fig. 13 and turns out to be approximately $\Delta h_{\text{bar}} \approx h/3$ based on the chosen calibration coefficients.

It can be seen that for this range of bar heights and depths, more than 80% of the expected wave conditions provide $\Delta h_{\text{min}} \leq \Delta h_{\text{bar}}$, and thus it is technically feasible to resolve these sand bars using phase speed depth inversions. Of course other field sites may have significantly different barred profile characteristics and if expected bar heights are smaller they may lie out of the observable range for a given site. In addition,

the chosen range of wave periods is probably somewhat wider than is usually observed over a given bar location on an active beach profile.

A slightly different approach is to identify the minimum bar height that can be observed as a function of wave conditions at a particular (unperturbed) water depth. Fig. 14 a) and b) show contours of minimum observable bar heights for depths of $h = 5$ m and 10 m, respectively. The figure indicates that minimum perturbation size increases rapidly with relative water depth (i.e. as wave period decreases). This is an expected result based on previous understanding of the linear dispersion relation (Dalrymple et al., 1998). However, for shallow relative depths (longer periods) there is a clear dependency on wave steepness (H/T) with minimum perturbation size increasing steadily with steepness. This reflects the fact that the sensitivity of wave phase speed to the local water depth decreases as the wave non-linearity of shallow water waves increases.

6. Conclusions

The objectives of the present study were to 1) assess the accuracy of a wide range of phase speed models when applied to non-linear, dispersive surf zone waves, and 2) quantify the potential improvement gained by incorporating non-linearity into phase speed-based depth inversions. A number of phase speed models were tested against laboratory observations, these models included those explicitly derived for linear, non-linear, breaking, and non-breaking waves. The observational data used for comparison consisted of very high-resolution remote sensing video along with in-situ surface elevation records. The analysis was focused on the surf zone, an area where previous depth inversion techniques have shown low skill. Nonetheless, the observational data consisted of waves exhibiting a range of non-linearity and dispersiveness.

The composite phase speed models (Kirby and Dalrymple, 1986; Booij, 1981) incorporate non-linear effects through the additional input of the local wave height and provided the best agreement with remotely measured phase speeds. Other models such as the bore and shock models, can at times show better local agreement. However, only at limited shallow water locations and their requirement of multiple water depth estimates as input parameters also severely hinders their use for depth inversions. The cnoidal wave model and a number of modified cnoidal models also performed relatively well. However, only when the locally measured wave heights were used was the phase speed agreement better than with linear dispersion.

Depth inversions using both linear theory and the KD86 composite model were performed in intermediate to shallow water ($0.15 < kh < 0.81$) for each of the individual monochromatic wave conditions. The median depth profiles were also calculated and these represent the net result from inverting speeds at individual frequencies (each with their own degree of non-linearity) for the same bathymetry. Under field conditions this is analogous to synchronous measurements of phase speeds at discrete frequencies in a random wave field. For inversions with the composite model, utilizing results from a

Table 4
Calibrated parameter space for the model of Hsu et al. (2006)

A_1	A_2	B_1	B_2	B_3
2.2	1.3	3.0	2.8	−0.5

five wave conditions reduced the errors from 20% to 10%, approximately.

As compared to linear theory, using the composite model significantly improved depth retrievals, with RMS errors for the median profile reduced from 30% to 10%. Overall, the inclusion of non-linearity allowed shallow water estimates to have the same or better accuracy as depth inversions performed in previous studies for intermediate water depths using linear dispersion. Considering the controlled conditions and extensive ground truth in the present analysis, this appears to be a practical limit for phase speed-based depth inversions.

Also, although only the composite model of KD86 was used for the depth inversions, both the KD86 and Booij (1981) models showed similar agreement to the phase speed observations for the present data set. It should be noted that the Booij (1981) model is simpler to invert and may be more useful in that sense in practical applications of the depth inversion technique. The two models may show more significant differences in high Ursell number and large relative water depth regimes (Hedges, 1987; Kirby and Dalrymple, 1987). However, this could not be tested with the present data set.

Finally, it was shown analytically that for the composite model the errors in retrieved depths are less sensitive to mea-

surement errors in the wave amplitude (as opposed to wavenumber errors). A phase speed sensitivity analysis also indicates that typical nearshore bathymetric features (bars or depressions), should be resolvable by depth inversions provided the remote sensing observations are sufficiently accurate and the range of existing wave conditions is sufficiently wide. Yet, the depth inversion problem is still fairly difficult and has a number of possible sources of error. In addition, it is of note that as wave steepness (H/T) increases in relatively shallow water, the sensitivity of the phase speed to bottom perturbations must necessarily decrease. Clearly, the overall accuracy of depth retrievals from inversion methods are decreased from traditional surveying methods; however, the cost savings and improvements in the speed of depth acquisition will still make inversion techniques useful in many situations.

Acknowledgments

The authors wish to thank the staff at the O.H. Hinsdale Wave Research Lab (HWRL) for the aid in conducting the experiments, including Dan Cox, Tim Maddux, Chris Scott, and Terry Dibble. We are also in debt to Rob Holman, John Stanley, Jason Killian, and Dan Clark of the Coastal Imaging Lab for establishing the ARGUS camera station at the HWRL, which was fundamental to this work. This work was partially supported by the Office of Naval Research under award number N00014-02-1-0147. P. Catalan was also supported by Departamento de Obras Civiles, Universidad Tecnica Federico Santa Maria, Chile.

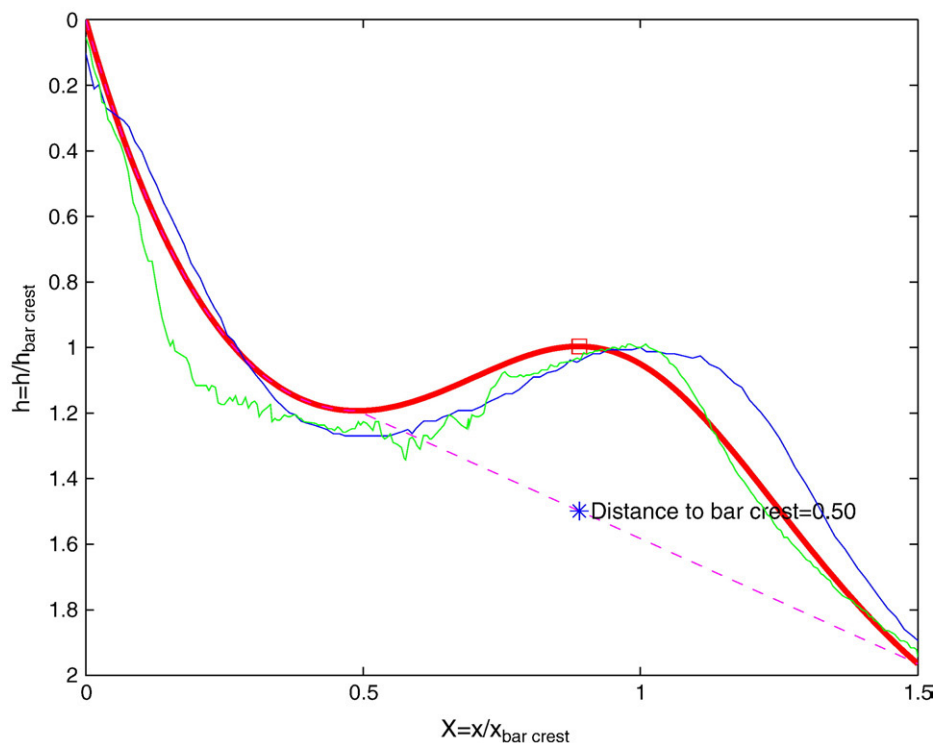


Fig. 15. Calibration of the model of Hsu et al. (2006) and determination of the relevant vertical distances. Red thick line is the calibrated model; thin lines correspond to the Duck profiles. Dashed magenta line correspond to the interpolated unperturbed profile. (For interpretation of the references to colour in this figure legend, the reader is referred to the web version of this article.)

Appendix A. Relative error for the composite model

By differentiating the KD86 model and performing some algebra, it is possible to obtain the relative error in water depth as a function of the relative error in wavenumber, frequency and wave amplitude:

$$\frac{\delta h}{h} = \frac{\delta \sigma}{\sigma} F_1(kh, A) - \frac{\delta k}{k} F_2(kh, A) - \frac{\delta A}{A} F_3(kh, A) \quad (\text{A.1})$$

with

$$F_1(kh, A) = \frac{2\Psi\Phi}{A_1 + \Psi(B_1 + C_1)\Phi} \quad (\text{A.2})$$

$$F_2(kh, A) = \frac{\Psi\Phi + (B_1 + C_1 + 2\varepsilon^2 D f_1)\Phi + (A_1 + A_2 \varepsilon f_2)\Psi}{A_1 \Psi + (B_1 + C_1)\Phi} \quad (\text{A.3})$$

$$F_3(kh, A) = \frac{2\varepsilon^2 D f_1 \Phi + A_2 \varepsilon f_2 \Psi}{A_1 \Psi + (B_1 + C_1)\Phi} \quad (\text{A.4})$$

where

$$\Phi = \tanh(kh + f_2 \varepsilon)$$

$$\Psi = (1 + f_1 \varepsilon^2 D)$$

$$\varepsilon = kA$$

$$f_1 = \tanh^5(kh)$$

$$f_2 = \left(\frac{kh}{\sinh(kh)} \right)^4$$

$$A_1 = A_2 \left(kh + \left(1 - 4\varepsilon f_2 kh \frac{\cosh(kh)}{\sinh(kh)} \right) \right)$$

$$A_2 = \text{sech}^2(kh + f_2 \varepsilon)$$

$$B_1 = 5kh\varepsilon^2 D \tanh^4(kh) \text{sech}^2(kh)$$

$$C_1 = \frac{f_1 \varepsilon^2}{2} kh \left(\frac{\sinh(4kh) - \tanh(kh) \text{sech}^2(kh)}{\sinh^4(kh)} - 8D \frac{\cosh(kh)}{\sinh(kh)} \right)$$

$$D = \frac{8 + \cosh(4kh) - 2\tanh^2(kh)}{8\sinh^4(kh)}$$

This expression collapses to that derived by Dalrymple et al. (1998) for the linear dispersion relation when $A=0$.

Appendix B. Calibration of the equilibrium beach profile

In order to characterize the typical bar height as a function of water depth, the equilibrium profile of Hsu et al. (2006) was calibrated with two barred profiles measured at the US Army Corp of Engineers Field Research Facility, in Duck, NC (www.frf.usace.army.mil/). In particular the profiles collected during October 11, 1990 and 1994 near $y=950$ m were used. The profiles were non dimensionalized by the depth and cross-shore coordinate at the bar crest, which enables a direct comparison with the model of Hsu et al. (2006), whose general expression is

$$H = A_1 (1 - \exp^{-B_1 X}) - A_2 \exp^{-B_3 (1-X)} \text{sech} B_2 (1 - X) + A_2 \exp^{-B_3} \text{sech} B_2, \quad (\text{B.1})$$

where $H=h/h_c$, $X=x/x_c$. The resulting parameter space is shown in Table 4 and the calibrated profile is shown in Fig. 15.

The next step is to determine the depth without the bar. It was found that the base term in the model of Hsu et al. (2006) yielded values that were too deep, in which case the bar height was about the same as the depth of the bar crest. Furthermore, this provided small values of Δh_{\min} allowing almost full observance of the bars. A more conservative value was obtained by interpolating between the bar trough and the point where $X=1.5$. Then, the depth of the imaginary point under the bar crest was determined and used to characterize the unperturbed depth. The resulting non-dimensional bar height was roughly half the depth of the bar crest for this particular set.

To convert these values to dimensional units, it is necessary to multiply it by the actual dimensional depth at the bar crest h_c . An empirical relation for this quantity as a function of the incident wave period and wave height was obtained by Hsu and Wang (1997) in the following form

$$\frac{h_c}{L_o} = 0.017 \xi_o^{-1.409} W_o^{-0.265}, \quad (\text{B.2})$$

where L_o , ξ_o and $W_o=H/(wT)$ are the deep water wavelength, Iribarren number and non-dimensional fall velocity. The average slope required to compute the Iribarren number was set to $\beta=0.035$ following Stockdon and Holman (2000), and a fall velocity of 1 cm/s was used. The above expression allows estimation of the bar height at any water depth.

References

- Aarninkhof, S., Ruessink, B.G., 2004. Video observations and model predictions of depth-induced dissipation. *IEEE Transactions on Geoscience and Remote Sensing* 42 (11), 832–844 (November).
- Aarninkhof, S.G.J., Ruessink, B.G., Roelvink, J.A., 2005. Nearshore subtidal bathymetry from time-exposure video images. *Journal of Geophysical Research* 110, C06011. doi:10.1029/2004JC002791.
- Abbot, M.B., Minns, A.W., 1992. *Computational hydraulics*, 2nd Edition. Ashgate Publishing Limited.
- Basco, D.R., 1985. A qualitative description of wave breaking. *Journal of Waterway, Port, Coastal, and Ocean Engineering* 111 (2), 171–188.
- Bell, P.S., 1999. Shallow water bathymetry derived from an analysis of X-band marine radar images. *Coastal Engineering* 37, 513–527.
- Bell, P.S., Williams, J.J., Clark, S., Morris, B.D., Vila-Concejo, A., 2004. Nested radar systems for remote coastal observations. *Journal of Coastal Research Special Issue* 39, 1.
- Bonneton, P., 2004. Wave celerity in the surf zone. *Proceedings, 29th International Conference on Coastal Engr. ASCE*, pp. 392–401.
- Booij, N., 1981. Gravity waves on water with non-uniform depth and current. *Tech. Rep. Rep. No.81-1*. Dept. Civ. Eng., Delft University of Technology.
- Buhr Hansen, J., Svendsen, I.A., 1979. Regular waves in shoaling water. Experimental data. *Tech. Rep. Ser. Pap. 21*, Inst. Hydrodyn. Hydraul. Eng. (ISVA), Tec. Univ. Denmark, Lyngby.
- Buhr Hansen, J., Svendsen, I.A., 1986. Experimental investigation of the wave and current motion over a longshore bar. *Proceedings, 20th International Conference on Coastal Engr. ASCE*, pp. 1166–1179.
- Catalán, P.A., 2005. Hybrid approach to estimating bathymetry using remote sensing. M.O.E Thesis, Oregon State University.
- Catalán, P.A., Haller, M.C., 2005. Nonlinear phase speeds and depth inversion. *Coastal Dynamics '05*. ASCE.
- Dalrymple, R.A., Kennedy, A.B., Kirby, J.T., Chen, Q., 1998. Determining depth from remotely sensed images. *Proceedings, 26th International Conference on Coastal Engr. ASCE*, pp. 2395–2408.
- Dankert, H., Rosenthal, W., 2004. Ocean surface determination from X-Band radar-image sequences. *Journal of Geophysical Research* 109, C04016. doi:10.1029/2003JC002130.

- Dingemans, M.W., 1997. Water wave propagation over uneven bottoms. *Advanced Series on Ocean Engineering*, vol. 13. World Sci., River Edge, N.J.
- Dugan, J.P., Piotrowski, C.C., Williams, J., 2001. Water depth and surface current retrievals from airborne optical measurements of surface gravity dispersion. *Journal of Geophysical Research* 106 (C8), 16903–16915.
- Flick, R.E., Guza, R.T., Inman, D.L., 1981. Elevation and velocity measurements of laboratory shoaling waves. *Journal of Geophysical Research* 86, 4149–4160.
- Grilli, S.T., Skourup, J., 1998. Depth inversion for nonlinear waves shoaling over a barred-beach. *Proceedings, 26th International Conference on Coastal Engr. ASCE*, pp. 603–616.
- Hedges, T.S., 1976. An empirical modification to linear wave theory. *Proceedings of the Institution of Civil Engineers* 61 (Part 2), 575–579 (Sep.).
- Hedges, T.S., 1987. Discussion: an approximate model for nonlinear dispersion in monochromatic wave propagation models, by J. T. Kirby and R. A. Dalrymple. *Coastal Engineering* 11, 87–89.
- Holland, T.K., 2001. Application of the linear dispersion relation with respect to depth inversion and remotely sensed imagery. *IEEE Transactions on Geoscience and Remote Sensing* 39 (11), 2060–2071.
- Hsu, T.-W., Wang, H., 1997. Geometric characteristics of storm beach profiles. *Journal of Coastal Research* 13 (4), 1102–1110.
- Hsu, T.-W., Tseng, I.-F., Lee, C.-P., 2006. A new shape function for bar-type beach profiles. *Journal of Coastal Research* 22 (3), 728–736 (May).
- Inman, D.L., Tait, R.J., Nordstrom, C.E., 1971. Mixing in the surf zone. *Journal of Geophysical Research* 76 (15), 3493–3514.
- Izquierdo, P., Nieto Borge, J., Guedes Soares, C., González, R.S., Rodríguez, G., 2005. Comparison of wave spectra from nautical radar images and scalar buoy data. *Journal of Waterway, Port, Coastal, and Ocean Engineering* 131 (3), 123–131.
- Kirby, J.T., Dalrymple, R.A., 1986. An approximate model for nonlinear dispersion in monochromatic wave propagation models. *Coastal Engineering* 9, 545–561.
- Kirby, J.T., Dalrymple, R.A., 1987. Discussion reply: an approximate model for nonlinear dispersion in monochromatic wave propagation models. *Coastal Engineering* 11, 89–92.
- Komar, P., 1998. *Beach Processes and Sedimentation*, second edition. Prentice Hall.
- Lippmann, T.C., Holman, R.A., 1991. Phase speed and angle of breaking waves measured with video techniques. *Coastal Sediments '91*, vol. 1, pp. 542–556.
- Madsen, P.A., Sørensen, O.R., Schäffer, H.A., 1997a. Surf zone dynamics simulated by a Boussinesq type model. Part I. Model description and cross-shore motion of regular waves. *Coastal Engineering* 32, 255–287.
- Madsen, P.A., Sørensen, O.R., Schäffer, H.A., 1997b. Surf zone dynamics simulated by a Boussinesq type model. Part II. Surf beat and swash oscillations for wave groups and irregular waves. *Coastal Engineering* 32, 289–319.
- Peregrine, D.H., 1967. Long waves on a beach. *Journal of Fluid Mechanics* 27, 815–827.
- Piotrowski, C.C., Dugan, J.P., 2002. Accuracy of bathymetry and current retrievals from airborne optical time series of imaging of shoaling waves. *IEEE Transactions on Geoscience and Remote Sensing* 40 (12), 2606–2618 (December).
- Puleo, J.A., Farquharson, G., Frasier, S.J., Holland, K.T., 2003. Comparison of optical and radar measurements of surf and swash zone velocity fields. *Journal of Geophysical Research* 108 (C3), 3100.
- Schäffer, H.A., Madsen, P.A., Deigaard, R., 1993. A Boussinesq model for waves breaking in shallow water. *Coastal Engineering* 20, 185–202.
- Scott, C.P., Cox, D.T., Maddux, T.B., Long, J.W., 2005. Large-scale laboratory observations of turbulence on a fixed barred beach. *Measurement Science and Technology* 16 (10), 1903–1912.
- Stansby, P.K., Feng, T., 2005. Kinematics and depth-integrated terms in surf zone waves from laboratory measurement. *Journal of Fluid Mechanics* 529, 279–310.
- Stansell, P., MacFarlane, C., 2002. Experimental investigation of wave breaking criteria based on wave phase speeds. *Journal of Physical Oceanography* 32, 1269–1283.
- Stive, M.J.F., 1980. Velocity and pressure field of spilling breakers. *Proceedings, 17th International Conference on Coastal Engr. ASCE*, pp. 547–565.
- Stive, M.J.F., 1984. Energy dissipation in waves breaking on gentle slopes. *Coastal Engineering* 8, 99–127.
- Stockdon, H.F., Holman, R.A., 2000. Estimation of wave phase speed and nearshore bathymetry from video imagery. *Journal of Geophysical Research* 105 (C9), 22015–22033.
- Suhayda, J.N., Pettigrew, N.R., 1977. Observations of wave height and wave celerity in the surf zone. *Journal of Geophysical Research* 82 (9), 1419–1424.
- Svendsen, I.A., 1974. Cnoidal waves over a gently sloping bottom. *Tech. Rep. Series Paper No. 6*. Institute of Hydrodynamics and Hydraulic Engineering, Technical University of Denmark.
- Svendsen, I.A., 2006. Introduction to Nearshore Hydrodynamics. *Advanced Series on Ocean Engineering*, vol. 24. World Sci., River Edge, N.J.
- Svendsen, I.A., Buhr Hansen, J., 1976. Deformation up to breaking of periodic waves on a beach. *Proceedings, 15th International Conference on Coastal Engr. ASCE*, pp. 477–496.
- Svendsen, I.A., Veeramony, J., 2001. Wave breaking in wave groups. *Journal of Waterway, Port, Coastal, and Ocean Engineering* 127 (6), 200–212.
- Svendsen, I.A., Madsen, P.A., Buhr Hansen, J., 1978. Wave characteristics in the surf zone. *Proceedings, 16th International Conference on Coastal Engr. ASCE*, pp. 520–539.
- Svendsen, I.A., Qin, W., Ebersole, B.A., 2003. Modeling waves at the LSTF and other laboratory facilities. *Coastal Engineering* 50, 19–45.
- Thornton, E.B., Guza, R.T., 1982. Energy saturation and phase speeds measured on a natural beach. *Journal of Geophysical Research* 87 (C12), 9499–9508.
- Thornton, E.B., Guza, R.T., 1983. Transformation of wave height distribution. *Journal of Geophysical Research* 88 (C10), 5925–5938.
- Walker, J.R., 1976. Refraction of finite-height and breaking waves. *Proceedings, 15th International Conference on Coastal Engr. ASCE*, pp. 507–524.
- Williams, W.W., 1946. The determination of gradients of enemy-held beaches. *Geographical Journal* 107, 76–93 (July).